SF2A 2015
F. Martins, S. Boissier, V. Buat, L. Cambrésy and P. Petit (eds)

SYSTEMATIC SPECTRAL ANALYSIS OF GX 339–4: EVOLUTION OF THE REFLECTION COMPONENT

M. Clavel[1], J. Rodriguez[1], S. Corbel[1] and M. Coriat[2]

Abstract. Black hole X-ray binaries display large outbursts, during which their properties are strongly variable. We develop a systematic spectral analysis of the 3–40 keV *RXTE*/PCA data in order to study the evolution of these systems and apply it to GX 339–4. Using a phenomenological model to account for the reflection process we provide a first overview of the evolution of the fluorescent iron line at 6.4 keV and of the associated smeared absorption edge at 7.1 keV, for all GX 339–4's outbursts monitored by the *RXTE* mission during its 16-year lifetime.

Keywords: accretion, accretion discs;, black hole physics, X-rays: binaries, Stars: individuals: GX 339–4

1 Introduction

Along the course of their large outbursts, the spectral shape of black hole X-ray binaries (BHXB) varies, tracing the evolution of a jet (or a corona), of an accretion disk and of the associated reflection processes. How these physical structures form and evolve over time is still under investigation (e.g. Remillard & McClintock 2006). To better constrain the theoretical models, one needs to compare the simulation outputs with the real observations, applying the same methods to both data sets. Therefore, we are developing a systematic procedure to reduce the *RXTE*/PCA data (Sec. 2) and to perform the corresponding spectral analysis (Sec. 3). In order to test our method and to obtain an initial set of generic spectral properties for BHXB, we use GX 339–4 which undergoes frequent outbursts, as prime example (e.g. Dunn et al. 2008). For this source, the spectral model chosen to account for the reflection processes is of great importance since an incomplete model can lead to the spurious detection of a high-temperature disk (Clavel et al. 2015). We present here a first overview of the reflection parameters we obtained using a phenomenological model including both a Gaussian iron line at 6.4 keV and the associated smeared absorption edge at 7.1 keV (Sec. 4).

2 RXTE/PCA observations and data reduction

GX 339–4's recurrent outbursts have been monitored with a large number of observatories at all wavelengths. In order to have a uniform spectral coverage over a maximum number of observations, we decided to restrict our systematic spectral analysis of GX 339–4 to the 3–40 keV *RXTE*/PCA data.

The *RXTE* mission operated from December 1995 to January 2012, providing a quasi-systematic follow-up of the X-ray binary outbursts over 16 years. We reduced all the 1389 Proportional Counter Array (PCA) observations available for GX 339–4*. We used the `HEASOFT` software suite v6.16 to reduce the corresponding data in a standard way, restricting it to the top layer of Proportional Counter Unit 2 (PCU2)†. We time-filtered the data, using *maketime* and *xtefilt*, to remove PCU2 breakdowns and to restrict it to the times when the elevation angle above the Earth is greater than 10°, and when the satellite pointing offset is less than 0.02°. The PCA response file was computed using *pcarsp* and the instrumental noise was estimated using *pcabackest*

[1] Laboratoire AIM, UMR 7158, CEA/CNRS/Univ. Paris Diderot, CEA DSM/IRFU/SAp, F-91191 Gif-sur-Yvette, France
[2] Université de Toulouse, UPS-OMP, CNRS, IRAP, 9 av. Colonel Roche, BP 44346, F-31028 Toulouse cedex 4, France

*This corresponds to all *RXTE*/PCA observations pointing within one degree from GX 339–4, ignoring slew and raster observations, as well as observations containing data gaps possibly affecting the data (obsIDs ending with G, T or U).

†PCU2 is the only unit which was active during all *RXTE* observations, and, for our study, the spectra are not significantly improved when adding the photon counts from PCU2's second and third layers.

with the background model pca_bkgd_cmbrightvle_eMv20051128.mdl. All observation/background spectra and average count rates were then extracted using *saextrct*. For PCA observations having a net average count rate lower than $40\,\mathrm{cts\,s^{-1}}$ over the full energy range, the instrumental background estimation was replaced by the one calculated from model pca_bkgd_cmfaintl7_eMv20051128.mdl. All spectra were binned in order to have at least 200 counts per resultant channel and a systematic error of 0.6% was added to account for instrumental uncertainties. In this work we present 3–10 keV lightcurves and spectral fits obtained in the 3–40 keV energy range. Following Clavel et al. (2015), we assume that the astrophysical background present in these data is negligible for observations having an average count rate over $0.77\,\mathrm{cts\,s^{-1}}$ in the 3–10 keV range. The observations having average count rates below this threshold are not considered further in this paper.

3 Spectral analysis

Following the method proposed by Dunn et al. (2010), we perform a systematic analysis of the 1260 spectra[‡] obtained for GX 339–4. For each observation, we test the presence of several spectral components using `XSPEC` software v12.8.2 models and chi-squared fitting routines, as well as parameter constraints discussed by Dunn et al. (2008), Plant et al. (2014) and Clavel et al. (2015).

3.1 Phenomenological model set

In addition to the non-thermal component modeled by an absorbed power law, PHABS×POWERLAW[§], we test the presence of a thermal emission coming from the accretion disk modeled by a multi-temperature blackbody EZDISKBB, and of a reflection component modeled by both a GAUSSIAN emission line and a smeared edge, SMEDGE. The latter component accounts for both the neutral iron absorption edge at 7.1 keV and the broad reflection hump, also called Compton hump, arising around 20 keV. Along with the Gaussian line, this component provides a sufficient model for the reflection process. Indeed, within the 3–40 keV range and with the *RXTE*/PCA energy resolution, this reflection model allows for good chi-square fits, it also prevents the detection of nonphysical parameters and gives results that are coherent with more-sophisticated self-consistent reflection models, such as XILLVER (Clavel et al. 2015; García et al. 2013). Our phenomenological model set can be summarized as follow,

$$\mathrm{phabs} \times (\mathrm{powerlaw} + \textit{ezdiskbb} + \mathbf{gaussian}) \times \mathbf{smedge} \tag{3.1}$$

where the disk component (in italic) and of the reflection component (in bold) are included only if they are statistically significant (see Sec. 3.2 for the model selection procedure). The column density corresponding to the photoelectric absorption PHABS is set to $\mathrm{N_H} = 0.4 \times 10^{22}\,\mathrm{cm^{-2}}$. The Gaussian line energy is fixed to $\mathrm{E_{line}} = 6.4\,\mathrm{keV}$, the SMEDGE threshold energy to $\mathrm{E_{edge}} = 7.1\,\mathrm{keV}$, its smearing width to $\mathrm{W} = 15\,\mathrm{keV}$ and the index for photoelectric cross section to $\mathrm{a} = -2.67$. All the other parameters (power law photon index Γ and normalization $\mathrm{I_{pwl}}$, disk maximal temperature $\mathrm{T_{max}}$ and normalization $\mathrm{I_{disk}}$, Gaussian normalization $\mathrm{I_{line}}$, edge maximum absorption factor at energy threshold τ_{max}) are left free to vary within physical ranges and are initialized at typical values in order to increase the chance of converging rapidly to a consistent fit.

3.2 Procedure to select the best fit model

Our systematic analysis performs the spectral fit of each observation with four models (POWERLAW, POWERLAW+REFLECTION, POWERLAW+DISK and POWERLAW+DISK+REFLECTION). We then identify the model having the best chi-square and use the `XSPEC` F-statistic test to check the statistical relevance of any optional components (i.e. any disk and/or reflection components), based on a comparison of chi-squares (χ^2) and degrees of freedom.

We are aware that the F-test we use is limited to data sets having a Gaussian statistic (which is the case considering the data large count rates and the consequent binning applied to the spectra, see Sec. 2) and cannot be used to test the presence of a Gaussian line (Protassov et al. 2002) nor of a multiplicative component

[‡]127 observations out of the 1389 we reduced are considered as dominated by the Galactic ridge emission and are therefore excluded from our spectral analysis (see Sec. 2 and Clavel et al. 2015). Two other observations also had to be ignored due to data reduction issues preventing a full spectral analysis.

[§]A model including a broken power law and/or a high energy cut-off, as tested by Dunn et al. (2010), are not statistically needed within the energy range of our analysis (3–40 keV).

(Orlandini et al. 2012). Therefore, similarly to what is done by (Dunn et al. 2010) we added a test on the iron line parameters: it is considered statistically relevant only if its normalization is at least $2\,\sigma$ above zero. When the emission line is detected, the edge should also be present in the spectrum. However, this multiplicative component may not be statistically needed for the fit. This is why we decide to include the SMEDGE in the best fit model only if the following two conditions are fulfilled: (i) the Gaussian line is required, (ii) the edge is significantly improving the overall fit (lowering the reduced χ^2 from more than 2.5 down to about 1).

The phenomenological models we are testing are quite simple. Therefore, for most of the observations, the best fit model selection can easily be done by eye. When this is the case, the automatic procedure gives results that are in good agreement with what one would expect. For this reason, we decide not to investigate for more complex statistical tests. Apart from few isolated observations (less than 1% of our sample), all best fit models have reduced χ^2 around 1 and the uncertainties we provide correspond to the $1\,\sigma$ error bars.

4 Standard spectral evolution of GX 339–4

Our data set is made of 1260 observations spread over the entire life time of the *RXTE* mission, sampling five major outbursts of GX 339–4 (see the source lightcurve and the corresponding hardness ratio in Fig. 1, panels A and B). These events all follow a standard cycle that can be summarized as follow: (i) an intensity rise in the hard state, best modeled by an absorbed power law, (ii) a transition to the soft state, with the detection of an additional disk component, (iii) an intensity decrease in the soft state, where the disk component is dominating the spectra, (iv) a transition back to the hard state, with the disappearance of the disk, and (v) an intensity decrease with a source remaining in the hard state.

Within these cycles, we identified the observations whose best fit models include a reflection component (Fig. 1, panel A). They correspond to the high count rate observations having a sufficient exposure time. This means that a relatively high statistic is needed to significantly detect the reflection component in a given spectrum. When this is the case, the iron line flux seems to follow the evolution of the source average count rate, starting from $\mathrm{I_{line}} \sim 10^{-4}\,\mathrm{ph\,cm^{-2}\,s^{-1}}$ for the lowest count rate observations ($\sim$20 cts s^{-1}) up to few $10^{-2}\,\mathrm{ph\,cm^{-2}\,s^{-1}}$ for the brightest ones (Fig. 1, panel C). In the hard state the smeared absorption edge is also statistically required and the corresponding maximum absorption factor is relatively stable with a typical value $\tau_{\max} \sim 1$. In the soft state this absorption component is not needed, likely because the higher energy part of the spectrum is then often poorly constrained. At the transitions between these two states, the smeared absorption edge is sometimes detected with a maximum absorption factor higher than 1.5 (Fig. 1, panel D). The origin of these extreme values is still under investigation but it could be associated to a disk component which is not detected by our systematic analysis. Indeed, these higher values are coupled with increasing values of the photon index (Clavel et al. 2015). If the later is fitting a soft excess in the spectrum, the absorption edge could then artificially create a break in the model, separating the soft and the hard components. This hypothesis will need to be tested using additional data from a broader energy range, in order to better constrain both the low and high energy parts of the GX 339–4 spectrum in the transition phases.

5 Conclusion

Our systematic analysis of the *RXTE*/PCA data between 3 and 40 keV highlights similar trends for all GX 339–4 outbursts, and it is important to disentangle the variations tracing the true evolution of the source from the one generated by the analysis itself. In this work we present a first overview of the evolution of the parameters related to the reflection model composed of an iron fluorescent line emission at 6.4 keV and of the associated smeared absorption edge at 7.1 keV. The first component is well defined in all observations having a sufficient statistic, while the second is mainly detected in the hard state. The absorption edge is also significantly required in part of the observations covering the transitions between the hard and soft states. However, for the latter observations, the high value of the absorption factor could also be due to the non-detection of a low-temperature disk component. Therefore, physical inputs on the source, as well as multi-wavelength observations, will be crucial to fully test our systematic analysis and to provide the generic properties of GX 339–4. This extensive study is beyond the scope of this paper and will be presented in a future publication (Clavel et al. in prep).

The authors acknowledge funding support from the French Research National Agency: CHAOS project ANR-12-BS05-0009 (http://www.chaos-project.fr).

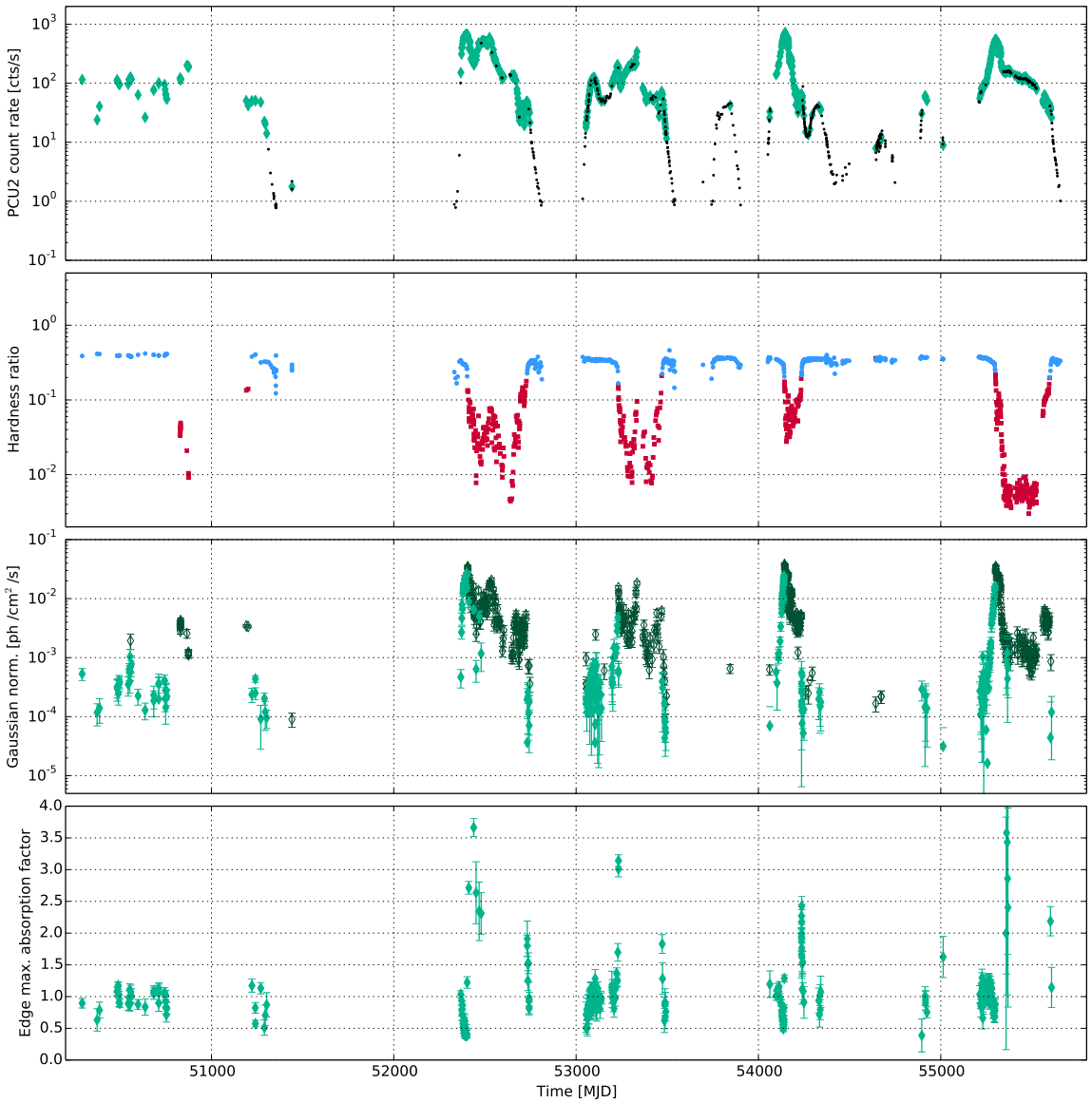

Fig. 1. *RXTE*/PCA lightcurve of all GX 339–4 observations having an average count rate above 0.77 cts s^{-1} and the best fit parameters related to the reflection component. From top to bottom: *(A)* 3–10 keV lightcurve with a color coding highlighting whether the observation best model includes a reflection component (green diamonds) or not (black dots); *(B)* The hardness ratio of each observation defined as the ratio of the 6–10 keV flux over the 3–6 keV one. The color coding highlights whether a disk component is statistically needed (red squares) or not (blue circles) ; *(C)* The intensity of the Gaussian emission line, whether the smeared absorption edge is statistically needed (green diamonds) or not (dark green empty diamonds); *(D)* The 7.1 keV maximum absorption of the SMEDGE component.

References

Clavel, M., Rodriguez, J., Corbel, S., & Coriat, M. 2015, AN, submitted
Dunn, R. J. H., Fender, R. P., Körding, E. G., Belloni, T., & Cabanac, C. 2010, MNRAS, 403, 61
Dunn, R. J. H., Fender, R. P., Körding, E. G., Cabanac, C., & Belloni, T. 2008, MNRAS, 387, 545
García, J., Dauser, T., Reynolds, C. S., et al. 2013, ApJ, 768, 146
Orlandini, M., Frontera, F., Masetti, N., Sguera, V., & Sidoli, L. 2012, ApJ, 748, 86
Plant, D. S., Fender, R. P., Ponti, G., Muñoz-Darias, T., & Coriat, M. 2014, MNRAS, 442, 1767
Protassov, R., van Dyk, D. A., Connors, A., Kashyap, V. L., & Siemiginowska, A. 2002, ApJ, 571, 545
Remillard, R. A. & McClintock, J. E. 2006, ARA&A, 44, 49